1
2
Top of the Atmosphere Reflected Shortwave Radiative Fluxes from GOES-R

4

5 Rachel T. Pinker[1], Yingtao Ma[1], Wen. Chen[1], Istvan Laszlo[2], Hongqing Liu[3],
6 Hye-Yun Kim[3] and Jamie Daniels[2]

7 [1] Department of Atmospheric and Oceanic Science, University of Maryland, College Park, MD

8 [2] NOAA NESDIS Center for Satellite Applications and Research, College Park, MD

9 [3] I.M. Systems Group, Inc., Rockville, MD

10 Correspondence to: Rachel T. Pinker (pinker@atmos.umd.edu)

11

12 **Abstract.** Under the GOES-R activity, new algorithms are being developed at the National Oceanic and
13 Atmospheric Administration (NOAA)/Center for Satellite Applications and Research (STAR) to derive
14 surface and Top of the Atmosphere (TOA) shortwave (SW) radiative fluxes from the Advanced Baseline
15 Imager (ABI), the primary instrument on GOES-R. This paper describes a support effort in the
16 development and evaluation of the ABI instrument capabilities to derive such fluxes. Specifically, scene
17 dependent narrow-to-broadband (NTB) transformations are developed to facilitate the use of observations
18 from ABI at the TOA. Simulations of NTB transformations have been performed with MODTRAN4.3
19 using an updated selection of atmospheric profiles and implemented with the final ABI specifications.
20 These are combined with Angular Distribution Models (ADMs), which are a synergy of ADMs from the
21 Clouds and the Earth's Radiant Energy System (CERES) and from simulations. Surface condition at the
22 scale of the ABI products as needed to compute the TOA radiative fluxes come from the International
23 Geosphere-Biosphere Programme (IGBP). Land classification at 1/6 $^\circ$ resolution for 18 surface types are
24 converted to the ABI 2-km grid over the (CONtiguous States of the United States) (CONUS) and
25 subsequently re-grouped to 12 IGBP types to match the classification of the CERES ADMs. In the
26 simulations, default information on aerosols and clouds is based on the ones used in MODTRAN.

27 Comparison of derived fluxes at the TOA is made with those from CERES and the level of agreement

28 for both clear and cloudy conditions is documented. Possible reasons for differences are discussed. The

29 product is archived and can be downloaded from the NOAA Comprehensive Large Array-data

30 Stewardship System (CLASS).

31

32 **Introduction**

33

34 One of the objectives at NOAA/STAR in respect to the utilization of observations from the Advanced

35 Baseline Imager (ABI) is to be able to derive shortwave (SW↓) radiative fluxes at the surface. To get to

36 the surface SW↓ from TOA satellite observations, there are two generic approaches: 1) the direct approach

37 and 2) the indirect approach. In the direct approach one uses all the necessary information needed for

38 deriving the surface fluxes (some of which can be derived from satellites). Implementation of such an

39 approach is feasible, for instance, with observations from MODIS which has a long history of product

40 availability and evaluation. Examples are illustrated in Wang and Pinker (2009), Niu and Pinker, (2015),

41 Ma et al. (2016), Pinker et al. (2018), Pinker et al., (2017a), Pinker et al. (2017b). GOES-R is a new

42 instrument and as yet, similar information to the one from MODIS is not available. Therefore, the indirect

43 approach is used where one starts from satellite observations at the TOA and models the atmosphere and

44 surface with best available information (which does not have to be based on ABI). Examples of such an

45 approach are discussed in Pinker, Zhang and Dutton (2005), Ma and Pinker (2012) and Zhang et al.

46 (2019). The "indirect path method" is used at the Center for Satellite Applications and Research (STAR)

47 (Laszlo et al., 2020) for deriving SW↓ radiative fluxes from satellite observations; it requires knowledge

48 of the SW broadband $(0.2 - 4.0\,\mu m)$ top of the atmosphere (TOA) albedo. The Advanced Baseline Imager

49 (ABI) observations onboard of the NOAA GOES-R series of satellites provide reflectance in six narrow

50 bands in the shortwave spectrum (**Table 1**); these must be first transformed into broadband reflectance

51 (the NTB conversion), and the broadband reflectance must be transformed into a broadband albedo (the

52 ADM conversion). During the pre-launch activity NTB transformations were developed based on

53 theoretical radiative transfer simulations with MODTRAN-3.7 and 14 land use classifications from the

2

International Geosphere-Biosphere Programme (*IGBP) (*Hansen et al., 2010*)*. They were augmented with ADMs from (CERES) observed ADMs (Loeb et al., 2003) and theoretical simulations (Niu and Pinker, 2011) to compute TOA fluxes. The resulting NTB transformations and ADMs have been tested using proxy data and simulated ABI data. The proxy instruments used in these early simulations include the GOES-8 satellite, the Advanced Very-High Resolution Radiometer (AVHRR) sensor on the Polar Orbiting satellites, the Spinning Enhanced Visible Infra-Red Imager (SEVIRI) sensor on the European METEOSAT Second Generation (MSG) satellites, and the Moderate Resolution Imaging Spectroradiometer (MODIS) instrument on the NASA Terra and Aqua Polar Orbiting satellites (Pinker et al*.,* 2021, unpublished). For each of these satellites, the evaluation of the methodologies was done differently; some results were evaluated against ground observations while others, against TOA information from CERES as well as from the (ESA) Geostationary Earth Radiation Budget (GERB) satellite (Harries et al., 2005). The results obtained provided an insight on the expected performance of the new ABI sensor. Those procedures have been subsequently updated and applied to the new ABI instrument once it was built and fully characterized.

This is a first paper that describes the development of a methodology to derive TOA SW fluxes from the Advanced Baseline Imager onboard the NOAA GOES-R series of geostationary satellites that are used at NOAA STAR as a starting point for deriving surface SW↓ fluxes. Evaluation of the methodology against best available estimates of TOA fluxes was also done. The TOA reflected SW flux is produced at NOAA together with the surface SW↓ flux and is archived at the NOAA Comprehensive Large Array-data Stewardship System (CLASS) at avl.class.noaa.gov. While the TOA reflected SW flux is a product on its own right, it is also a prerequisite to deriving the SW↓ surface flux; as such, versions for TOA and surface have the same labeling. The methodology will be presented in section 2, data used are described in section 3, results in section 4 and a summary and discussion in section 5.

81 **2. Methodology**

82

83 The following two flowcharts (**Figs. 1 and 2**) describe the necessary steps to derive the NTB

84 transformations and the ADMs. Details on these two steps will follow.

85 The TOA narrowband and broadband reflectance can be calculated from the spectral radiances

86 simulated from MODTRAN 4.3 and the response functions of the satellite sensor as shown in equations

87 (1) and (2):

88
$$\rho_{nb}(\theta_0,\theta,\phi) = \frac{\pi \int_{\lambda 1}^{\lambda 2} I(\lambda,\theta_0,\theta,\phi)G(\lambda)d\lambda}{\int_{\lambda 1}^{\lambda 2} \cos(\theta_0)S_0(\lambda)G(\lambda)d\lambda} \qquad (1)$$

89
$$\rho_{bb}(\theta_0,\theta,\phi) = \frac{\pi \int_{0.2\,\mu m}^{4\,\mu m} I(\lambda,\theta_0,\theta,\phi)d\lambda}{\int_{0.2\,\mu m}^{4\,\mu m} \cos(\theta_0)S_0(\lambda)d\lambda} \qquad (2)$$

90

91 Where:

92 ρ_{nb} : is narrowband reflectance;

93 ρ_{bb} : is broadband reflectance;

94 θ_0: solar zenith angle;

95 θ : view (satellite) zenith angle; ϕ : relative azimuth angle;

96 I_λ : reflected spectral radiance; $S_0(\lambda)$: solar spectral irradiance;

97 G_λ : spectral response functions of satellite sensors; λ_1 and λ_2 are the spectral limits of the sensor spectral

98 band. This approach is widely used in the scientific community as also implemented in the work of Loeb

99 et al (2005), Wielicki et al. (2008), Su et al. (2015) and Akkermans et al. (2020).

4

100   As stated previously, the ADMs from CERES-based observations (Loeb et al., 2005; Kato et al. 2015)

101   were augmented with theoretical simulations (Niu and Pinker, 2011) to compute TOA fluxes. This was

102   done since CERES observations at that time were under-sampled at higher latitudes.

103   The combined ADMs are developed for each angular bin by weighting the modeled and CERES ADMs

104   based on the number of samples used to derive the ADMs of each type (Niu et al., 2011). Specifically:

105 $$\bar{R}(\theta_0,\theta,\phi) = \frac{1}{m+n}\left(m \times R_{CERES}(\theta_0,\theta,\phi) + n \times R_S(\theta_0,\theta,\phi)\right) \qquad (3)$$

106     $\bar{R}(\theta_0,\theta,\phi)$:   averaged ADMs at each angular bin;

107   R_{CERES}:   anisotropic factor from CERES ADMs;

108   R_S: anisotropic factor from simulated ADMs;

109   m and n: observation numbers at angular bins for CERES and simulated ADMs.

110

111 **2.1 Selection of Atmospheric profiles for simulations**

112

113   We have selected 100 atmospheric profiles covering the globe and the seasons as input for simulations

114   with MODTRAN4.3. The atmospheric profiles at each pressure level include temperature, water vapor

115   and ozone. Each season includes 25 profiles. A tool was developed to select profiles from a Training Data

116   set known as SeeBor Version 5.0 (https://cimss.ssec.wisc.edu/training_data/) (Borbas et.al. 2005).

117   Originally it consisted of 15704 global profiles of temperature, moisture, and ozone at 101 pressure levels

118   for clear sky conditions. The profiles are taken from NOAA-88, and the European Centre for Medium-

119   Range Weather Forecasts (ECMWF) 60L training set, TIGR-3, ozone-sondes from 8 NOAA Climate

120   Monitoring and Diagnostics Laboratory (CMDL) sites, and radiosondes from the Sahara Desert during

121   2004. A technique to extend the temperature, moisture, and ozone profiles above the level of existing data

was also implemented by the providers (University of Wisconsin-Madison, Space Science and Engineering Center, Cooperative Institute for Meteorological Satellite Studies (CIMSS). **Fig. 3** shows the location of the selected profiles.

The SeeBor profiles are clear sky profiles. The top of the profiles is at 0.005 mb which is about 82.6 km. We did an experiment to check the impact of reducing the number of levels for a profile (initially, we have used only 40 levels). In the experiment computed were radiances from profiles with 50 levels as well as radiances from profiles with 98 Levels. The difference between the two radiances (50 lev-98 lev) were below 5 % reaching 15 % around 2.5 μm. In the experiment we used the odd number levels starting from surface (plus the highest level) to reduce the number of profile levels. Based on these experiments we have opted to keep all 98 profile levels.

The surface variables we have used are from MODIS and include surface skin temperature, 2 m temperature, land/sea mask, and albedo. We have conducted a thorough investigation how the selected profiles represent the entire sample of 15704 profiles. An example showing the comparison of temperature, humidity and ozone profiles is shown in **Fig. 4.** As seen, there is a positive bias in the selected profile of temperature due to their higher concentration at the lower latitudes. A positive bias can be found at the lower levels while a negative bias is seen above 1 mb. Since our domain of study is in such latitudes this selection should not have adverse effects on the simulations performed.

2.2 Surface conditions

Surface condition is one of the primary inputs into the MODTRAN simulations. The International Geosphere-Biosphere Programme (IGBP) land classification is used as a source (Hansen et al., 2010; Loveland et al., 2010). The dataset is at 1/6-degree resolution and includes 18 surface types. We have converted the 1/6º (~18.5 km) resolution to the ABI 2-km grid using the nearest grid method **(Fig. 5)**. The surface type is fixed in time. The method for cloudy sky uses 4 surface types; these are also derived from 12 IGBP types (**Table 2**).

2.3 Clear and cloudy sky simulations

Under clear sky, scattering from aerosols is important. We have included 6 aerosol types (**Table 3**) to cover a range of possible conditions under clear sky. Aerosol models are selected based on the type of extinction and a default meteorological range for the boundary-layer aerosol models as listed below:

Aerosol Type 1: Rural extinction, visibility = 23 km

Aerosol Type 4: Maritime extinction, visibility = 23 km

Aerosol Type 5: Urban extinction, visibility = 5 km

Aerosol Type 6: Tropospheric extinction, visibility = 50 km

Aerosol Type 8: Advective Fog extinction, visibility = 0.2 km

Aerosol Type 10: Desert extinction for default wind conditions

For the 6 aerosol types, the total number of MODTRAN simulations for each surface type is 462,000. It is obtained as follows: 6 aerosol types x 100 profiles x 770 angles.

When performing NTB simulations, we use all 6 types of aerosols. The Rural, Ocean, Urban and Fog aerosols are distributed in the lower 0-2 km region. Tropospheric aerosol is distributed from 0 to 10 km tropopause. The Rural, Ocean, Urban and Tropospheric aerosol optical properties have Relative Humidity (RH) dependency. The Single Scattering Albedo (SSA) is given on 4 RH grids (0, 70, 80, 99) on a spectral grid of 788 points ranging from 0.2 to 300 microns.

Simulations were performed for ABI for all the cloud cases described in **Table 3.** To merge cloud layers with atmospheric profiles we have followed the procedure as described in *Berk et al.* (1985, 1998), namely: "Cloud profiles are merged with the other atmospheric profiles (pressure, temperature, molecular constituent, and aerosol) by combining and/or adding new layer boundaries. Any cloud layer boundary within half a meter of an atmospheric boundary layer is translated to make the layer altitudes coincide; new atmospheric layer boundaries are defined to accommodate the additional cloud layer boundaries." 100% relative humidity is assumed within the cloud layers (default).

2.4 Selection of angles

The total number of angles used in the simulations is given in **Table 4**. The selected spectral grids for solar zenith angles, satellite view angles and relative azimuth angles are at Gaussian quadrature points, plus 0° to solar zenith angles (sza) and satellite viewing angles (vza) and 0° and 180° (forward and backward view) to the satellite relative azimuth angles. Solar angle and satellite view angle are referenced to target or surface for satellite simulation with 0° meaning looking up (zenith). Relative azimuth angle is defined as when the relative azimuth angle equals 180°, the sun is in front of observer.

The definitions of solar zenith angle and azimuth angle in this table corresponds to the definitions of MODTRAN but that is not the case for the satellite zenith angle. MODTRAN uses nadir angle as 180°-satellite zenith angle, ignoring spherical geometry.

2.5 Selection of optimal computational scheme

MODTRAN4.3 provides three multiple scattering models (Isaacs, DISORT, and Scaled Isaacs) and three band models at resolutions (1 cm^{-1}, 5 cm^{-1}, and 15 cm^{-1}). The DISORT model (Stamnes et al.*,* 1988) provides the most accurate radiance simulations but the runs are very time consuming. The Isaacs (Isaacs et al. 1987) 2-stream algorithm is fast but oversimplified. The Scaled Isaacs method performs radiance calculations using Isaacs 2-stream model over full spectral range and using DISORT model at a small number of atmospheric window wavelengths. The multiple scattering contributions for each method are identified and ratios of the DISORT and Isaacs methods are computed. This ratio is interpolated over the full wavelength range, and finally, applied as a multiple scattering scale factor in a spectral radiance calculation performed with the Isaacs method.

To optimize simulation speed and accuracy, we performed various sensitivity tests, including combinations of multiple scattering models, band resolution, and number of streams. **Table 5** lists simulation options and their corresponding calculation speed.

202 Based on results presented in **Table 5**, the efficient options (< 40 seconds) are Isaacs, DISORT 2-stream

203 with 15 cm^{-1}, DISORT 4-stream 15 cm^{-1}, and Scaled Isaacs all streams at all resolutions. Although the

204 ideal option is DISORT 8-stream with 1 cm^{-1} resolution, there is a trade-off between speed and accuracy.

205 **Fig. 6** compares DISORT simulated radiances at three band resolutions. We use two spectral ranges of

206 0.4 – 0.5 µm and 1.5 – 2.0 µm to illustrate differences. **Fig. 6** shows that the coarser band resolution has

207 smoothed out the radiance variations. The 15 cm^{-1} has the smoothest curve among the three, and 1 cm^{-1}

208 shows more variations than the other two. Another (scientific) criteria for selecting the spectral resolution

209 is the ability to resolve/match the relative spectral response function (SRF) of a sensor. For example, the

210 SRFs of channels 1-6 of ABI are given at every 1 cm^{-1}.

211 Accordingly, we have chosen the 1 cm^{-1} band model for the MODTRAN radiance simulations. Performed

212 were also radiance simulations from different multiple scattering models at 1 cm^{-1} resolution. The whole

213 spectrum of 0.2 – 4 µm was separated to 14 sections so that the differences can be assessed clearly. For

214 wavelength below 0.3 µm and beyond 2.5 no discernible differences were found among Isaacs, DISORT

215 2-, 4-, and 8-strem, and Scaled Isaac. The largest differences occurred in the spectral range of 0.4 – 1.0

216 µm. Scaled Isaac 8-stream follows DISORT 8-stream closely across the whole spectral range; the Scaled

217 Isaac method provided near-DISORT accuracy with the speed of Isaacs. Thus, the MODTRAN4.3

218 simulations for GOES-R ABI were set-up with Scaled Isaac 8-stream with 1 cm^{-1} band resolution.

219 For illustration, in **Fig. 7** compared are radiances simulated by Isaac 2 stream, Scaled Isaac, and DISORT-

220 4 stream for the case of Relative Azimuthal Angle=1.9^{o}, View Angle=76.3^{o}, Solar Zenith Angle=87.2^{o}.

221 The lines are differences between various settings and DISORT-8 stream (e.g. Isaacs minus DISORT-8).

222 Isaac has the least accuracy since it is oversimplified, 4-stream showed some improvements when

223 compared with Isaac while still has large differences for 0.4 µm and is still computationally demanding.

224 Scaled Isaac provides the smallest differences between DISORT-8. **Fig. 7** (lower) zoomed in to the large

225 difference area of 0.3-0.35 µm which indicates that Scaled Isaacs still provides satisfactory results.

226

227

228

2.6 Regression methodologies

We have derived coefficients of regression using a constrained least-square curve fitting methods of Matlab, "lsqnonneg", which can solve a linear or nonlinear least-squares (data-fitting) problem and produce non-negative coefficients. Non-negative coefficients avoid generating negative TOA flux, which is not a physically valid.

To ensure that information from all channels is used and avoid the complex cross-correlation problem, it was opted to generate Narrow to Broad (NTB) coefficients for each ABI channel separately. These channel specific NTB coefficients are applied to each channel to convert ABI narrow-band reflectance to extended band. The final broad-band TOA reflectance is taken as the weighted sum of all 6-channel specific broad-band reflectance. The logic behind this approach is the assumption that the narrow-band reflectance from each channel is a good representative for a limited spectral region centered around the channel and the total spectral reflectance is dominated by the spectral region that contains the most solar energy.

To generate "separate-channel" NTB coefficients, each narrow-band ABI channel reflectance is converted to a reflectance $\rho_{bb,i}$ separately,

$$\rho_{bb,i}(\theta_0, \theta, \phi) = c_{0,i}(\theta_0, \theta, \phi) + c_{1,i}(\theta_0, \theta, \phi) * \rho_{nb,i}(\theta_0, \theta, \phi) \qquad (4)$$

where $\rho_{bb,i}$ is the band reflectance for an interval around each channel i; $c_{0,i}$ and $c_{1,i}$ are regression coefficients for channel i. These regression coefficients are derived separately for various combination of surface, cloud and aerosol types. The total shortwave broad band $(0.25 - 4.0\mu m)$ reflectance ρ_{bb}^{est} is obtained by taking the weighted sum of all 6 $\rho_{bb,i}$ reflectance

$$\rho_{bb}^{est}(\theta_0, \theta, \phi) = \sum_i \rho_{bb,i}(\theta_0, \theta, \phi) \frac{S_{0,i}}{S_0} \qquad (5)$$

Here, S_0 and $S_{0,i}$ are total solar irradiance and band solar irradiance for each channel, respectively. Band edges around the six ABI channels are: 49980-18723, 18723-13185, 13185-9221, 9221-6812, 6812-5292, 2500 cm^{-1} 0.2001-0.5341, 0.5341-0.7584, 0.7584-1.0845, 1.0845-1.4680, 1.4680-1.8896, 1.8896-4.0000 µm). The corresponding solar irradiance band values are 364, 360, 287, 168, 91, 87

10

255   W m^{-2}. **Fig. 8** shows the sensor response function (SRF) and locations of the six ABI channels.

256   Coefficients are generated for clear condition and 3 types of cloudy conditions. Comparison between ABI

257   TOA flux and CERES products are shown in **Fig. 9**. The "separate-channel" coefficients work well for

258   predominantly clear sky (**Fig.10**). Differences are somewhat more scattered for cloudy cases. The reason

259   may be due to the fact that the ABI observation time and CERES product time do not match perfectly

260   since cloud condition change quickly. As discussed in Gristey et al. (2019) there are SW spectral

261   reflectance variations for different cloud types. Possibly, for ABI bands some spectral variations

262   associated with cloud variability are missed. It is important to have the correct cloud properties to be able

263   to select correct ADM. Misclassification of cloud properties will therefore result in flux differences. They

264   also argue that ADMs have an uncertainty due to within-scene variability and within-angular bin

265   variability leading to additional flux differences.

266

267   **3. Data used**

268

269   **3.1 Satellite data for GOES-16 and GOES-17**

270

271   The Advanced Baseline Imager (ABI) data used (Table 6) were downloaded from the NOAA

272   Comprehensive Large Array-Data Stewardship System (CLASS) at

273   https://www.avl.class.noaa.gov/saa/products/welcome. Both level 1b (L1b) and level 2 (L2) data were

274   used. These can be found by searching the CLASS site by selecting "GOES-R Series ABI Products

275   GRABIPRD (partially restricted L1b and L2+ Data Products)". The L1b data included the radiances

276   (RadC) in files "OR_ABI-L1b-RadC-MmCnn_G1SS_stime_etime_ctime, where "m", "nn" and "SS"

277   indicate the ABI scan mode, channel number (01-06) and satellite identification number (16 or 17),

278   respectively. "stime", and "etime" are the start and end dates and times of the scan, "ctime" is the date

279   and time the file was created. The ABI L2 product used were the clear-sky mask, cloud top phase, cloud

280   optical depth. The names of these files are constructed similarly to the L1b radiance files, except that the

281   radiance product name RadC is replaced by ACMC, ACTPC, CODC and AODC, respectively, and the

282 reference to the channel number is omitted. For example, GOES-16 with ABI operating in scan mode 6

283 in the CONUS domain, the name of the clear-sky mask file is OR_ABI-L2-ACMC-M6_G16_

284 stime_etime_ctime. (In the product names above the letter C indicates the CONUS domain.)

285 The clear-sky mask product consists of a binary cloud mask identifying pixels as clear, probably clear,

286 cloudy or probably cloudy. The cloud top phase product provides cloud classification identification

287 information for each pixel. The cloud phase categories are clear sky, liquid water, super cooled liquid

288 water, mixed phase, ice, and unknown. The cloud optical depth product gives the optical thickness along

289 an atmospheric column for each pixel. All products have a nominal sub-satellite spatial resolution of 2

290 km.

291

292 When searching the NOAA CLASS site, go to "GOES-R Series ABI Products GRABIPRD (partially

293 restricted L1b and L2+ Data Products)". The SRF are downloaded from

294 https://ncc.nesdis.noaa.gov/GOESR/ABI.php.

295

296 **3.2 Reference data from CERES**

297

298 The CERES Single Scanner Footprint (SSF) is a unique product for studying the role of clouds, aerosols,

299 and radiation in climate. Each CERES footprint (nadir resolution 20-km equivalent diameter) on the SSF

300 includes reflected shortwave (SW), emitted longwave (LW) and window (WN) radiances and top-of-

301 atmosphere (TOA) fluxes from CERES with temporally and spatially coincident imager-based radiances,

302 cloud properties, and aerosols, and meteorological information from a fixed 4-dimensional analysis

303 provided by the Global Modeling and Assimilation Office (GMAO). Each file in this data product

304 contains one hour of full and partial-Earth view measurements or footprints at a surface reference level.

305 Detailed information can be found via https://ceres.larc.nasa.gov/data/#ssf-level-2 (we used version 4a)

306 Near real-time CERES fluxes and clouds in the SSF format are available within about a week of

307 observation (Kratz et al., 2014). They do not use the most recent CERES instrument calibration and thus

308   contains some uncertainty. Before GOES data were transferred to the Comprehensive Large Array-data

309   Stewardship System (CLASS) system, the NOAA/STAR archive was holding new data for about a week.

310   Therefore, the initial evaluations had to be done only with data that overlapped in time. The CERES data

311   known as the FLASHFlux Level2 (FLASH_SSF) are available almost in real time from:

312   https://ceres.larc.nasa.gov/products.php?product=FLASHFlux-Level2 (we used version 3c).

313   Due to such constraints the early comparison was done between ABI data as archived at NOAA/STAR

314   and the FLASHFlux products (in this paper, the FLASHFlux data were used only in Fig. 9). The archiving

315   of GOES-R at the NOAA Comprehensive Large Array-data Stewardship System (CLASS) started only

316   in 2019, however, it contains data starting from 2017. Once the CLASS archive became available, we

317   have augmented GOES-16 cases with observations from GOES-17; only those cases will be shown in this

318   paper.

319

320   **3.3 Data preparation**

321

322   For the re-mapping, we adopted the ESMF re-gridding package. The detailed information can be found

323   at: http://earthsystemmodeling.org/regrid/

324   For an ideal situation, the ABI high-resolution TOA SW fluxes should be mapped into the CERES

325   footprint for validation. However, there are reasons that make it difficult to do so. There can be more than

326   18000 pixels in a single swath of the SSF, when constrained to U.S. Different pixels have different times.

327   Neglecting the seconds, there are still more than 30 mins differences (this changes case by case) between

13

328   the first pixel and the one at the end and this brings up a time matching issue. By remapping the SSF to

329   ABI, we can set up a unique time for ABI (ABI is at 5 min intervals) and then constrain the region and

330   the time range of SSF.

331   Both re-mapping the ABI to SSF and remapping SSF to the ABI bring up spatial matching errors as

332   recognized by the scientific community (Rilee and Kuo, 2018; Ragulapati et al., 2021). In **Fig. 11**, we

333   show the SSF before re-gridding (**Figs 11 (a) & (b)**) and after re-gridding (**Figs. 11 (c) and (d)).** The

334   fluxes after re-mapping CERES SSF to the ABI resolution resemble well the original structure. Another

335   consideration is the computational efficiency of re-mapping the curvilinear tripolar grid to unconstructed

336   grid. For large arrays, it is more efficient to remap the unconstructed grid to the curvilinear tripolar grid.

337

338   **4. Results**

339

340   **4.1 Comparison between ABI TOA fluxes to those from CERES SSF**

341

342   A case for 2019/12/26 (doy 360) UTC 19:36 is illustrated in **Figs. 11-14.** Statistical summaries from an
343   extended number of cases that cover all four seasons are presented in **Table 7**.
344   We have conducted several experiments to select an appropriate regression approach to the NTB
345   transformation ensuring that non-physical results are not encountered. Based on the samples used in this
346   study **(Table 7)** the differences found for Terra and GOES-16 were in the range of -0.5-(-17.37) for bias
347   and 43.28-81.72 for standard deviation; for Terra and GOES-17 they were 11.26-47.09 and 70.25-108.73,
348   respectively. For Aqua and GOES-16 they were 7.63-33.87and 58.68-117.43 respectively while for Aqua
349   and GOES-17 they were 0.19-31.53 and 47.55-129.42, respectively (all units are W m^{-2}). The evaluation
350   process revealed the challenges in undertaking such comparisons. Both estimates of TOA fluxes (CERES

351 and GOES) do no account for seasonality in the land use classification; the time matching for the different

352 satellites is important and limits the number of samples that can be used in the comparison. Based on the

353 results of this study recommendation for future work include the need to incorporate seasonality in land

354 use and spectral characteristic of the various surface types. Possible stratification by season in the

355 regressions could also be explored.

356

357 **4.2 Causes for differences between ABI and CERES TOA fluxes**

358

359 **4.2.1 Differences in surface spectral reflectance**

360

361 In the MODTRAN simulations we use the spectral reflectance information on various surface types as

362 provided by MODTRAN. MODTRAN version 4.3.1 contains a collection of spectral surface reflectance

363 dataset from the Moderate Spectral Atmospheric Radiance and Transmittance (MOSART) model

364 (Cornette et al., 1994) and others from Johns Hopkins University Spectral Library (Baldridge et al., 2009).

365 When doing simulation, we call the built-in surface types and use the provided surface reflectance. As

366 such, the spectral dependence of the surface reflectance used in the simulations and matched to the

367 CERES surface types may not be compatible with the classification of CERES. Also, seasonal changes

368 in surface type classification can introduce errors due to changes in the spectral surface reflectance for

369 different surface types (**Fig. 15).**

370

371 **4.2.2 Issues related to surface classification**

372

373 Another possible cause for differences between the TOA fluxes is the classification of surface types as

374 originally identified by the IGBP and used in the simulations. No seasonality is incorporated in the surface

375 type classification while such variability is part of the CERES observations.

376

377

15

4.2.3 Issues related to match-up between GOES-R and CERES

Both Terra and Aqua have sun-synchronous, near-polar circular orbits. Terra is timed to cross the equator from north to south (descending node) at approximately 10:30 am local time. Aqua is timed to cross the equator from south to north (ascending node) at approximately 1:30 pm local time. The periods for Terra and Aqua are 99 and 98 minutes, respectively. Both have 16 orbits per day. CERES on Terra and Aqua optical FOV at nadir is 16 x 32 or 20 km resolution. Terra passes CONUS during 03-06 UTC (US night time), 16-20 UTC (US day time), and Aqua passes CONUS during 07-11 UTC (US night time), 18-22 UTC (US day time).

Both Terra and Aqua have an instantaneous FOV values at SWATH level. There is no perfect overlap, temporally or spatially with ABI data. The ABI radiance and cloud data are on a regular grid of 2*2 km over CONUS at each hour. To use CERES data for evaluation of ABI, there is a need to perform collocation in both time and space.

5. Summary

The derivation and evaluation of TOA radiative fluxes as simulated for any given instrument are quite challenging. In principle, there is a need to account for all possible changes in the atmospheric and surface conditions one may encounter in the future. Yet, to know what these conditions are at the time of actual observation when there is a need to select the appropriate combination of variables from the simulations, is a formidable task. Differences in assumed cloud properties can also lead to differences in the fluxes derived from the two instruments. Therefore, error can be expected due to discrepancies between the actual conditions and the selected simulations and these are difficult to estimate. The approach we have selected is based on high-quality simulations using a proven and accepted radiative transfer code (MODTRAN) of known configurations and a wide range of atmospheric conditions. We have also selected the best available estimates of TOA radiative fluxes from independent sources for evaluation. However, the matching between different satellites in space and time is challenging. In selecting the cases

for evaluation, we have adhered to strict criteria of time and space coincidence as described in section 3.3.

Critical elements of an inference scheme for TOA radiative flux estimates from satellite observations are:

1) transformation of narrowband quantities into broadband ones;

2) transformation of bi-directional reflectance into albedo by applying Angular Distribution Models (ADMs). In principle, the order in which these transformations are executed is arbitrary. However, since well established, observation-based broadband ADMs derived from the Clouds and the Earth's Radiant Energy System (CERES) project already exist, the logical procedure is to do the NTB transformation on the radiances first, and then apply the ADM. This is the sequence that has been followed here. While the road map to accomplish above objectives seems well defined, reaching the final goal of having a stable up-to-date procedure for deriving TOA radiative fluxes from a new instrument like the ABI on the new generation of GOES satellites is quite complicated. Since the final configuration of the instrument becomes known at a much later stages the evaluation of new algorithms is in a fluid stage for a long time so early evaluation against "ground truth" needs to be repeated frequently. Additional complication is related to the lack of maturity of basic information needed in the implementation process, such as a reliable cloud screened product which in itself is in a process of development and modifications. The "ground truth", namely, the CERES observations are also undergoing adjustments and recalibration. As such, the process of deriving best possible estimates of TOA radiative fluxes from ABI underwent numerous iterations to reach its current status. An effort was made to deal the best way possible with the fluid situation. All the evaluations against CERES were repeated once the ABI data reached stability and were archived in CLASS and we used the most recent auxiliary information. This study sets the stage for future possible improvements. One example is land classification which currently is static. Another issue is related to the representation of real time aerosol optical properties which are important under clear sky conditions. It is believed that only now when NOAA/STAR has a stable aerosol retrieval algorithm, it would be timely to address the aerosol issue in the estimation of TOA fluxes under clear sky.

Data availability. The data are available upon request from the corresponding author.

451

452

Reference:

Akkermans T., and Clerbaux, N.: Narrowband-to-Broadband Conversions for Top-of-Atmosphere
Reflectance from the Advanced Very High-Resolution Radiometer (AVHRR),
Remote Sens. 12 (2), 305; https://doi.org/10.3390/rs12020305, 2020.

Berk, A., Bernstein, L. W., and Robertson, D. C.: MODTRAN: A moderate resolution model for
LOWTRAN 7, Philips Laboratory, Report AFGL-TR-83-0187, Hanscom AFB, MA, 1985.

Berk, A., G. P. Anderson, P. K., Acharya, D. C. Robertson, J. H. Chetwynd, S. M. Adler-Golden:
MODTRAN Cloud and Multiple Scattering Upgrades with Application to AVIRIS, Remote Sensing
of Environment, 65 (3), 367-375, https://doi.org/10.1016/S0034-4257(98)00045-5, 1998.

Baldridge, A. M., Hook, S. J., Grove, C. I., Rivera, G.: The ASTER spectral library version 2, Remote
Sensing of Environment 113, doi: 10.1016/j.rse.2008.11.007, 2009.

Borbas, E. E., Seemann, S. W., Huang, H.-L., Li, J., and Menzel, W. P.: Global profile training database
for satellite regression retrievals with estimates of skin temperature and emissivity. Proceedings of
the XIV, International ATOVS Study Conference, Beijing, China, University of Wisconsin-
Madison, Space Science and Engineering Center, Cooperative Institute for Meteorological Satellite
Studies (CIMSS), Madison, WI, pp.763-770, 2005.

Clerbaux, N., Russell, J. E., Dewitte, S., Bertrand, C., Caprion, D., De Paepe, B., Sotelino, L. G., Ipe, A.,
Bantges, R., and Brindley, H. E.: Comparison of GERB instantaneous radiance and flux products
with CERES Edition-2 data, Rem. Sens. of Environ., **113**, 102-114. doi:
10.1016/j.rse.2008.08.016, 2009.

Cornette, W. M., Acharya, P. K., Robertson, D. C., and Anderson, G. P.: Moderate Spectral Atmospheric
Radiance and Transmittance Code *(MOSART)*, Rep. R-057-94 (11–30), La Jolla, CA: Photon
Research Associates, 1994.

Gristey, J. J., Su, W., Loeb, N. G., Vonder Haar, T. H., Tornow, F., Schmidt, K. S., Hakuba, M. Z.,

Pilewskie, P., Russell, J. E.: Shortwave Radiance to Irradiance Conversion for Earth Radiation Budget Satellite Observations: A Review, Remote Sens. 13, 2640, https://doi.org/10.3390/rs13132640, 2021.

Kato, S., Loeb, N. G., Rutan, D. A., Rose, F. G.: Clouds and the Earth's Radiant Energy System (CERES) Data Products for Climate Research Journal of the Meteorological Society of Japan, 93 (6), 597−612, DOI:10.2151/jmsj.2015-048, 2015.

Kratz, D. P., Stackhouse Jr., P. W., Gupta, S. K., Wilber, A. C., Sawaengphokhai, P., and McGarragh, G. R.: The Fast Longwave and Shortwave Flux (FLASHFlux) Data Product: Single-Scanner Footprint Fluxes, J. Appl. Meteor. Climatology, 53, 1059-1079, doi: 10.1175/JAMC-D-13-061.1, 2014.

Hansen, M. C., Defries, R. S., Townshend, J. R. G., and Sohlberg, R.: Global land cover classification at 1km spatial resolution using a classification tree approach, International Journal of Remote Sensing, 21(6-7):1331 – 1364, DOI:10.1080/014311600210209 https://doi.org/10.1080/014311600210209, 2010.

Harries, J. E., Russell, J. E., Hanafin, J. A., Brindley, H., Futyan, J., Rufus, J., Kellock, S., G. Matthews, R. Wrigley, A. Last, J. Mueller, R. Mossavati, J. Ashmall, E. Sawyer, D. Parker, M. Caldwell, P M. Allan, A. Smith, M. J. Bates, B. Coan, B. C. Stewart, D. R. Lepine, L. A. Cornwall, D. R. Corney, M. J. Ricketts, D. Drummond, D. Smart, R. Cutler, S. Dewitte, N. Clerbaux, L. Gonzalez, A. Ipe,C. Bertrand, A. Joukoff, D. Crommelynck, N. Nelms, D. T. Llewellyn-Jones, G. Butcher, G. L. Smith, Z. P Szewczyk, P E. Mlynczak, A. Slingo, R. P. Allan, and M. A. Ringer: The Geostationary Earth Radiation Budget Project, Bull. Amer. Meteor. Soc. 86 (7): 945, doi: 10.1175/BAMS-86-7-945, 2005.

Isaacs, R. G., W.-C. Wang, R. D. Worsham, and S. Goldenberg, S.: Multiple scattering LOWTRAN and FASCODE models. Applied Optics, 26(7), 1272 – 1281, 1987.

Kato, S., and Loeb, N. G.: Top-of-atmosphere shortwave broadband observed radiance and estimated irradiance over polar regions from Clouds and the Earth's Radiant Energy System (CERES) instruments on Terra, J. Geophys. Res., 110, D07202, doi:10.1029/2004JD005308, 2005.

504 Laszlo, I., Liu, H., Kim, H.-Y., and Pinker, R. T. : GOES-R Advanced Baseline Imager (ABI) Algorithm
505   Theoretical Basis Document (ATBD) for Downward Shortwave Radiation (Surface), and Reflected
506   Shortwave Radiation (TOA), version 3.1, Available at https://www.goes-r.gov/resources/docs.html,
507   2018.

508 Laszlo, I., Liu, H., Kim, H.-Y., and Pinker, R. T.: Shortwave Radiation from ABI on the GOES-R Series,
509   in: *The GOES-R Series*, edited by S. J. Goodman, T. J. Schmit, J. Daniels and R. J. Redmon. 179-191,
510   Elsevier, doi: https://doi.org/10.1016/B978-0-12-814327-8.00015-9, 2020.

511 Loeb, N. G., Smith, N. M., Kato, S., Miller, W. F., Gupta, S. K., Minnis, P. and Wielicki, B. A.: Angular
512   Distribution Models for Top-of Atmosphere Radiative Flux Estimation from the Mission Satellite,
513   Part I: Methodology, Journal of Applied Meteorology, 42 240-265, 2003.

514 Loeb N. G. et al.: Angular distribution models for top-of- atmosphere radiative flux estimation from the
515   Clouds and the Earth's Radiant Energy System Instrument on the Terra satellite. part I:
516   Methodology. J. Atmos. Oceanic Technol., 22:338–351, 2005.

517 Loveland T. R., B. C. Reed, J. F. Brown, D. O. Ohlen, Z. Zhu, L. Yang, J. W. Merchant: Development
518   of a global land cover characteristics database and IGBP DISCover from 1 km AVHRR data,
519   International Journal of Remote Sensing, 21 (6-7), 1303-1330, 2010.

520 Ma, Y., R. T. Pinker, M. M. Wonsick, C. Li, and L. M. Hinkelman: Shortwave radiative fluxes on
521   slopes. JAMC, 55, 1513-1532, https://doi.org/10.1175/*JAMC*-D-15-0178.1, 2016.

522 Ma, Y. and Pinker, R. T.: Shortwave Radiative Fluxes from Satellites: An Update. J. Geophys. Res.
523   Atmos**.**, 117, Issue D23, DOI: 10.1029/2012JD018332, 2012.

524 Niu, X. and Pinker, R. T.: Revisiting satellite radiative flux computations at the top
525   of the atmosphere, International Journal of Remote Sensing, DOI:10.1080/01431161.2011.571298,
526   2011.

527 Niu, X. and Pinker, R. T.: An improved methodology for deriving high resolution
528   surface shortwave radiative fluxes from MODIS in the Arctic region, J. Geophys. Res.
529   Atmos., 120, 2382–2393, doi: 10.1002/2014JD022151, 2015.

530 Pinker, R. T., Zhang B., Dutton E. G.: Do satellites detect trends in surface solar radiation? *SCIENCE*,
531   308, 5723, 850-854, 2005.

532 Pinker, R. T., A. Bentamy, B. Zhang, W. Chen, and Ma, Y.: The net energy budget at the ocean-
533   atmosphere interface of the ''Cold Tongue'' region, J. Geophys. Res. Oceans, 122, doi: 10.1002/
534   2016JC012581, 2017a.

535 Pinker, R. T., S. Grodsky, B. Zhang, A. Busalacchi, and Chen, W.: ENSO Impact on Surface Radiative
536   Fluxes as Observed from Space. J. Geophys. Res.-Oceans., doi: 10.1002/2017JC012900, 2017b.

537 Pinker, R. T., Zhang, B. Z., Weller, R. A., and Chen, W.: Evaluating surface radiation fluxes observed
538   from satellites in the southeastern Pacific Ocean. Geophysical Research Letters, 45.
539   https://doi.org/10.1002/2017GL076805, 2018.

540 Rajulapati, C. R., S. M. Papalexiou, M. P. Clark, and Pomeroy, J. W.: The Perils of Regridding:
541   Examples Using a Global Precipitation Dataset, Journal of Applied Meteorology and
542   Climatology, 60 (11), 1561–1573, doi: 10.1175/JAMC-D-20-0259.1, 2021.

543 Rilee M. L. and Kuo, K. S.: The Impact on Quality and Uncertainty of Regridding Diverse Earth
544   Science Data for Integrative Analysis, IN43C-0916, 2018.

545 Scarino et al.: A Web-Based Tool for Calculating Spectral Band Difference Adjustment Factors Derived
546   from SCIAMACHY Hyperspectral Data, IEEE Trans. Geo. Remote Sens., 54, 5,
547   10.1109/TGRS.2015.2502904, 2016.

548 Stamnes, K., S.-C. Tsay, W. Wiscombe and K. Jayaweera: Numerically stable algorithm for discrete-
549   ordinate-method radiative transfer in multiple scattering and emitting layered media, Applied
550   Optics, 27 (12), 2502–2509, 1988.

551 Su, W., Corbett, J., Eitzen, Z., and Liang, L.: Next-generation angular distribution models for
552   top-of-atmosphere radiative flux calculation from CERES instruments: methodology, Atmos.
553   Meas. Tech., 8, 611–632, https://doi.org/10.5194/amt-8-611-2015, 2015.

554 Wang, H; Pinker, R. T.: Shortwave radiative fluxes from MODIS: Model development and
555   implementation. JGR-Atmospheres, 114, D20201, 2009.

556　Wielicki, B. A.; Doelling, D. R.; Young, D. F.; Loeb, N. G.; Garber, D. P.; MacDonnell, D. G.: Climate

557　　　　quality broadband and narrowband solar reflected radiance calibration between sensors in orbit.

558　　　　In Proceedings of the IGARSS 2008 IEEE International Geoscience and Remote Sensing

559　　　　Symposium, Boston, MA, USA, 7–11 July 2008.

560　Zhang, T., Stackhouse Jr., P. W., Cox, S. J., Mikovitz, J. C., Long, C. N.: Clear-sky shortwave

561　　　　downward flux at the Earth's surface: Ground-based data vs. satellite-based data, Journal of

562　　　　Quantitative Spectroscopy & Radiative Transfer, 224, 247-260, 2019,

563　　　　www.elsevier.com/locate/jqsrt.

564
565
566
567

Tables

Table 1. Channel information and spectral bands for ABI.

ABI Band #	Central wavelength (μm)	Spectral band (μm)
1	VIS 0.47	0.45-0.49
2	VIS 0.64	0.60-0.68
3	NIR 0.86	0.847-0.882
4	NIR 1.38	1.366-1.380
5	NIR 1.61	1.59-1.63
6	NIR 2.26	2.22-2.27

568

569

570

571 Table 2. Surface classification description for IGBP 18 types, IGBP 12 types, CERES clear sky 6 types,

572   and NTB cloudy sky 4 types

IGBP (18 types)	IGBP (12 types)	CERES clear-sky (6 types)	NTB cloudy-sky (4 types)
Evergreen Needleleaf	Needleleaf Forest	Mod-High Tree/Shrub	Land
Deciduous Needleleaf			
Evergreen Broadleaf	Broadleaf Forest		
Deciduous Broadleaf			
Mixed Forest	Mixed Forest		
Closed Shrublands	Closed Shrub		
Woody Savannas	Woody Savannas		
Savannas	Savannas	Low-Mod Tree/Shrub	
Grasslands	Grasslands		
Permanent Wetlands			
Tundra			
Croplands	Croplands		
Open Shrublands	Open Shrub		
Urban and Built-up	Open Shrub	Dark Desert	Desert
Bare Soil and Rocks	Barren and Desert	Bright Desert	
Snow and Ice	Snow and Ice	Snow and Ice	Snow and Ice
Water Bodies	Ocean	Ocean	Water

573
574
575

576

577   Table 3. The various classes for which NTB coefficients are generated.

Parameter	Clear condition	Cloudy condition
Aerosol or cloud type	6 aerosol types (rural, maritime, urban, tropospheric, fog, desert)	3 cloud types (cirrus, stratocumulus, altostratus)
Optical depth (OD)	Typical VIS (km) values for each aerosol types (no OD grid for each aerosol type). Rural: 23, maritime: 23, urban: 5, tropospheric: 50, fog: 0.2, desert: (default VIS for wind speed 10m/s)	Cirrus: [0, 0.8, 1.2, 1.8, 3.2] Stratocumulus: [0, 0.8, 1.2, 1.8, 3.2, 5.8, 8.2, 15.8, 32.2, 51.8, 124.2] Altostratus: [0, 15.0, 30.0, 50.0, 80.0]
Surface type	12 IGBP surface types	4 types (Water, Land, Desert, Snow/Ice)

578

579

580

581

582 Table 4. Angles used in simulations. To be consistent with what is presented in the

583   ABI Shortwave Radiation Budget (SRB) Algorithm Theoretical Basis Documents (ATBD) (Laszlo

584   et al, 2018) the additional angles used in the simulations are not given in this Table.

Angle Type	Angles
Solar Zenith Angle [°]	0.0, 12.9, 30.8, 41.2, 48.3, 56.5, 63.2, 69.5, 75.5, 81.4, 87.2
Satellite Zenith Angle [°]	0.0, 11.4, 26.1, 40.3, 53.8, 65.9, 76.3
Azimuth Angle [°]	0.0, 1.9, 10.0, 24.2, 44.0, 68.8, 97.6, 129.3, 162.9, 180

585

586

587

588

589

Table 5. MODTRAN simulation speed test (CPU MHz 2099.929).

Algorithm	Stream	Band Resolution (cm^{-1})	Speed (~seconds)
Isaacs	2	1	40
DISORT	2	1, 5, 15	280, 70, 30
	4	1, 5, 15	560, 120, 40
	8	1, 5, 15	930, 300, 110
Scaled Isaac	2	1, 5, 15	30, 10, 6.67
	4	1, 5, 15	30, 10, 6.67
	8	1, 5, 15	30, 10, 6.67

590

591

592

593

594 Table 6. Details on data used as input for calculations.
595

Short Name	Long Name	MODE	ABI-Channel	Scan Sector	Spatial Resolution
RadC	L1b Radiance	M6	C01-C06	CONUS	5000x3000
AODC	L2 Aerosol	M6	--	CONUS	2500x1500
ACMC	L2 Clear Sky Masks	M6	--	CONUS	2500x1500
ACTPC	L2 Cloud Top Phase	M6	--	CONUS	2500x1500
CODC*	L2 Cloud Optical Depth	M6	--	CONUS	2500x1500

596

597 *The CODC data were not always available from CLASS and had to be obtained from NOAA/STAR

598 temporary archives. Also, not all the required angular information needed for implementation of the

599 regressions is available online and had to be re-generated.

600

601

602   Table 7. Statistical summary for all selected cases inter-compared at instantaneous time scale.

Case	CERES	GOES-R	Corr	Bias	Std	RMSE	N
07/31 2019 UTC 19	Terra	G16	0.82	0.81	69.81	69.81	0.22×10^6
		G17	0.87	29.13	90.10	94.70	1.78×10^6
	Aqua	G16	0.76	33.87	117.43	122.22	1.58×10^6
		G17	0.78	31.53	129.42	133.21	0.29×10^6
09/13 2019 UTC 20	Terra	G16	0.87	-17.37	81.72	83.54	0.13×10^6
		G17	0.71	47.09	108.73	118.48	1.73×10^6
	Aqua	G16	0.76	18.22	108.50	110.02	1.46×10^6
		G17	0.73	25.14	81.95	85.72	0.53×10^6
09/21 2019 UTC 19	Terra	G16	0.85	6.78	66.66	67.00	0.35×10^6
		G17	0.83	26.41	87.64	91.57	1.75×10^6
	Aqua	G16	0.82	29.66	105.09	109.20	1.67×10^6
		G17	0.76	6.03	94.70	94.89	0.15×10^6
09/30 2019 UTC 19	Terra	G16	0.88	4.49	64.79	64.94	0.40×10^6
		G17	0.80	19.35	86.41	88.55	1.74×10^6
	Aqua	G16	0.80	19.87	100.45	102.40	1.69×10^6
		G17	0.72	2.71	91.79	91.83	0.12×10^6
	Terra	G16	0.86	5.84	51.44	51.77	0.35×10^6

10/23 2019 UTC 19		G17	0.87	22.47	70.25	73.76	1.75×10^6
	Aqua	G16	0.89	17.10	75.95	77.85	1.67×10^6
		G17	0.78	8.98	72.52	73.07	0.15×10^6
11/08 2019 UTC 19	Terra	G16	0.87	-0.50	43.28	43.28	0.35×10^6
		G17	0.82	17.18	71.27	73.31	1.75×10^6
	Aqua	G16	0.90	10.08	71.27	71.98	1.67×10^6
		G17	0.68	1.53	47.55	47.58	0.15×10^6
11/24 2019 UTC 19	Terra	G16	0.79	7.98	49.10	49.75	0.35×10^6
		G17	0.87	14.10	78.35	79.61	1.76×10^6
	Aqua	G16	0.82	7.63	58.68	59.17	1.67×10^6
		G17	0.65	0.19	63.14	63.14	0.15×10^6
12/26 2019 UTC 19	Terra	G16	0.88	5.24	53.28	53.54	0.35×10^6
		G17	0.76	11.26	73.95	74.80	1.76×10^6
	Aqua	G16	0.83	9.79	58.90	59.56	1.67×10^6
		G17	0.73	0.85	52.53	52.54	0.15×10^6

603
604
605
606
607
608
609
610
611

612   List of Figures

638 Figure 13. Same as Figure 11 but for clear TOA SW differences.

639 Figure 14. Same as Figure 11 but for cloudy TOA SW differences.

640 Figure 15. *Left:* Sensor response function for ABI channel 6; *Right:* Spectral albedo for desert and open

641   shrubs. Desert albedo value is much higher than open shrubs at 2.2 µm.

642

643
644
645

646

647
648
649
650
651
652
653
654
655
656
657
658
659
660
661
662
663
664
665
666
667
668
669
670
671
672
673

674
675
676 **Figures**
677
678

```
┌─────────────────────────────────────────────┐
│  Geometry Data (SZA, VZA, AZA),              │
│  Atmospheric Information (ozone, water vapor, │
│  aerosols, clouds), and Surface Condition    │
│  (spectral reflectance)                       │
└─────────────────────────────────────────────┘
                      │
            ┌──────────────────┐
            │   Run MODTRAN     │
            └──────────────────┘
                      │
        ┌──────────────────────────┐
        │  Obtain TOA directional   │
        │    spectral radiance      │
        └──────────────────────────┘
                      │                    ┌──────────────────┐
                      │◄───────────────────│  Apply Satellite  │
                      │                    │ Sensor Spectral   │
                      │                    │ Response Function │
                      │                    └──────────────────┘
        ┌──────────────────────────┐
        │  Calculate TOA narrowband │
        │      and broadband        │
        │      reflectances         │
        └──────────────────────────┘
                      │
        ┌──────────────────────────┐
        │   Establish NTB conversion│
        │      relationships        │
        └──────────────────────────┘
                      │
        ┌──────────────────────────┐
        │   Obtain NTB conversion   │
        │      coefficients         │
        └──────────────────────────┘
                      │
              ╭──────────────╮
              │   End NTB      │
              ╰──────────────╯
```
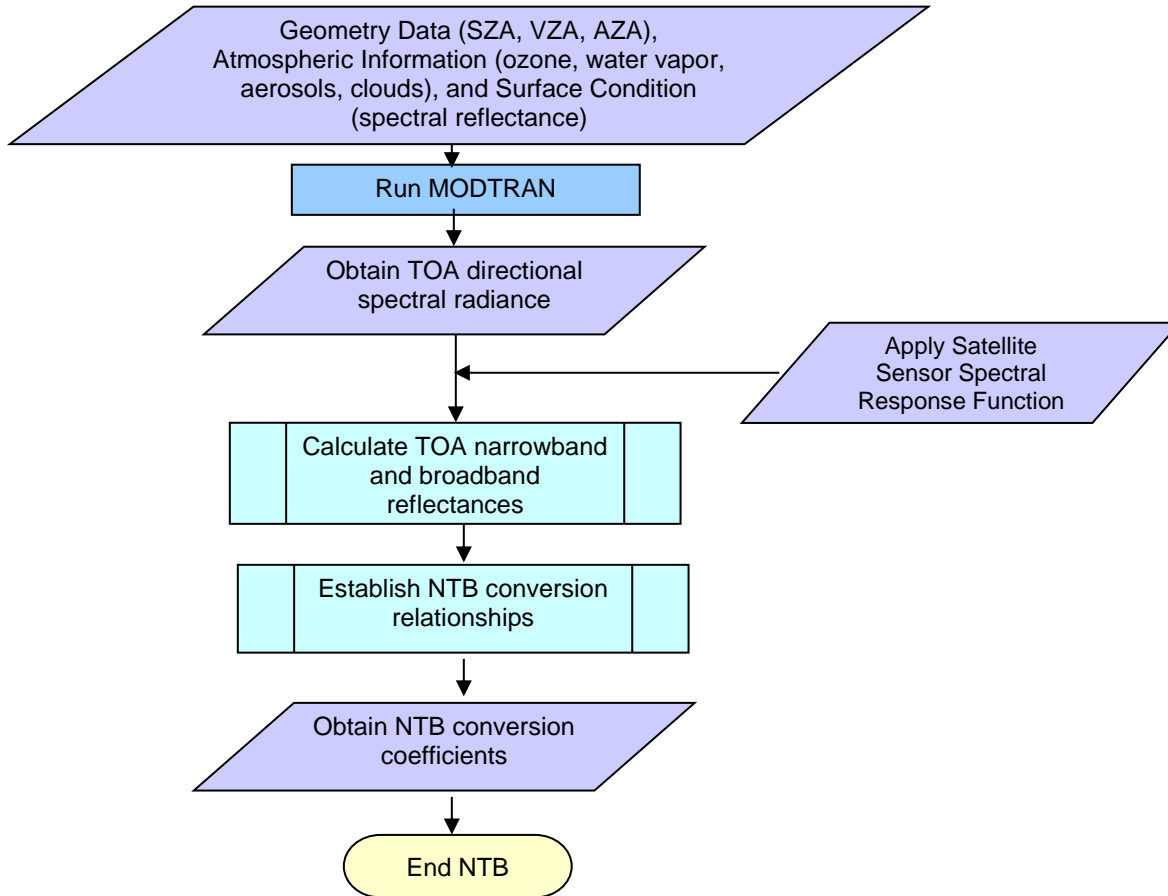
679
680 Figure 1. Flowchart of the NTB transformations illustrating the main processing sections.
681
682
683
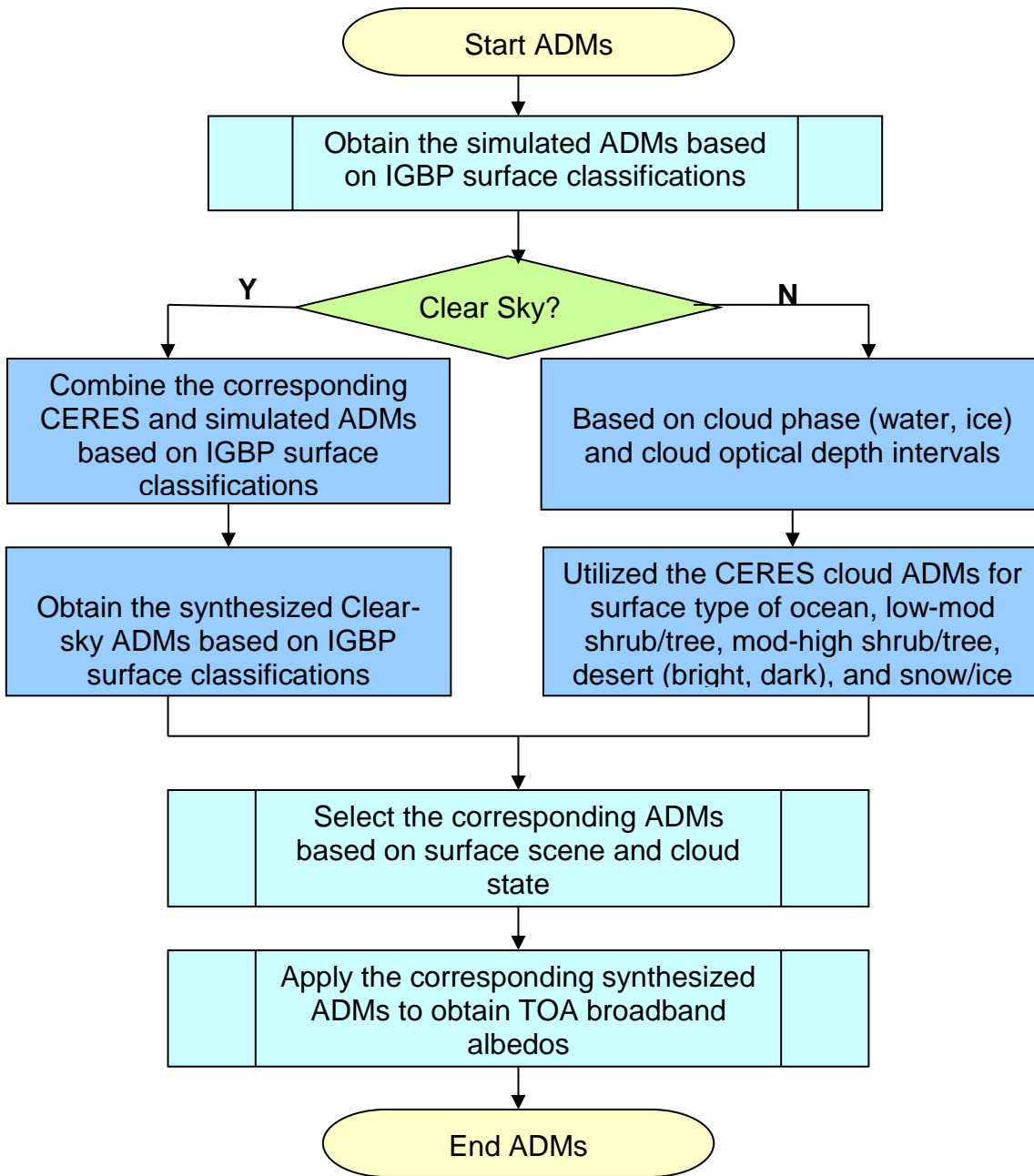
684

685   Figure 2. Schematic illustration of the logic employed to synthesize modeled and observed ADMs.

686

687

688

689

690
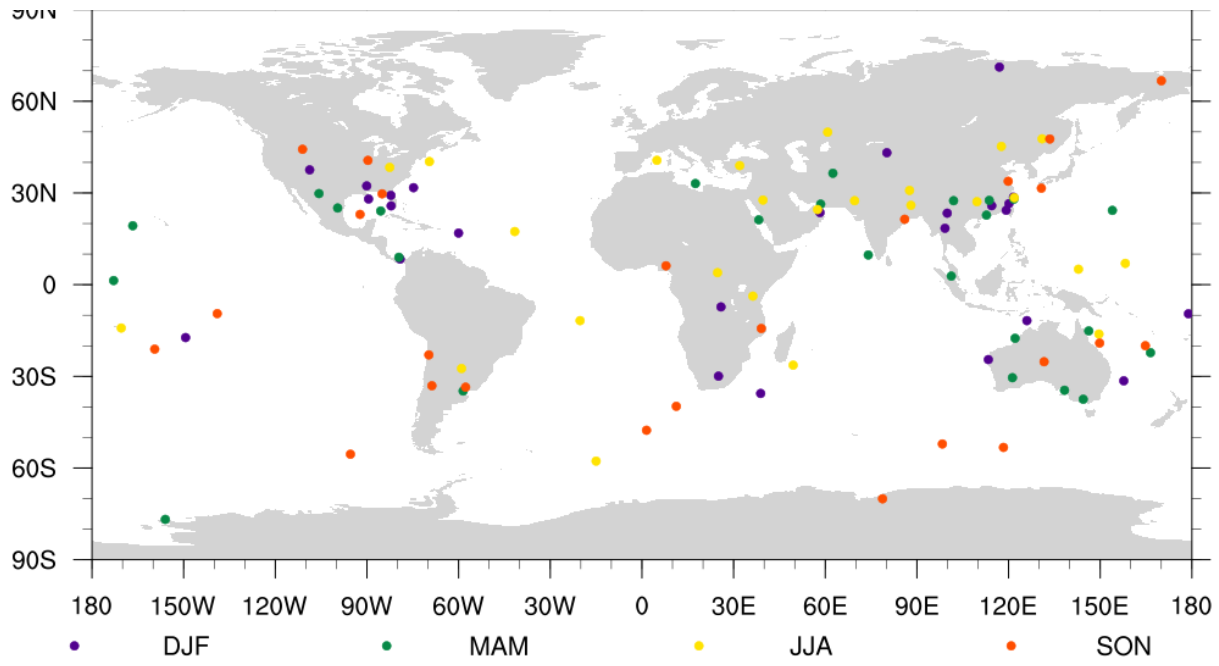
Figure 3. The location of the 100 selected clear sky profiles from SeeBor used in the simulations.

692

693

694
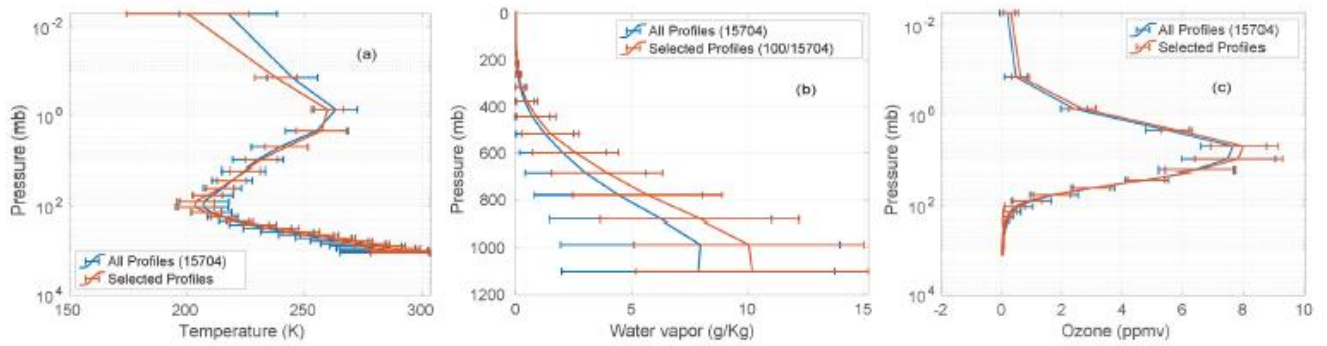
Figure 4. Profile statistics of: (a) temperature; (b): water vapor; (c) ozone for the entire available sample
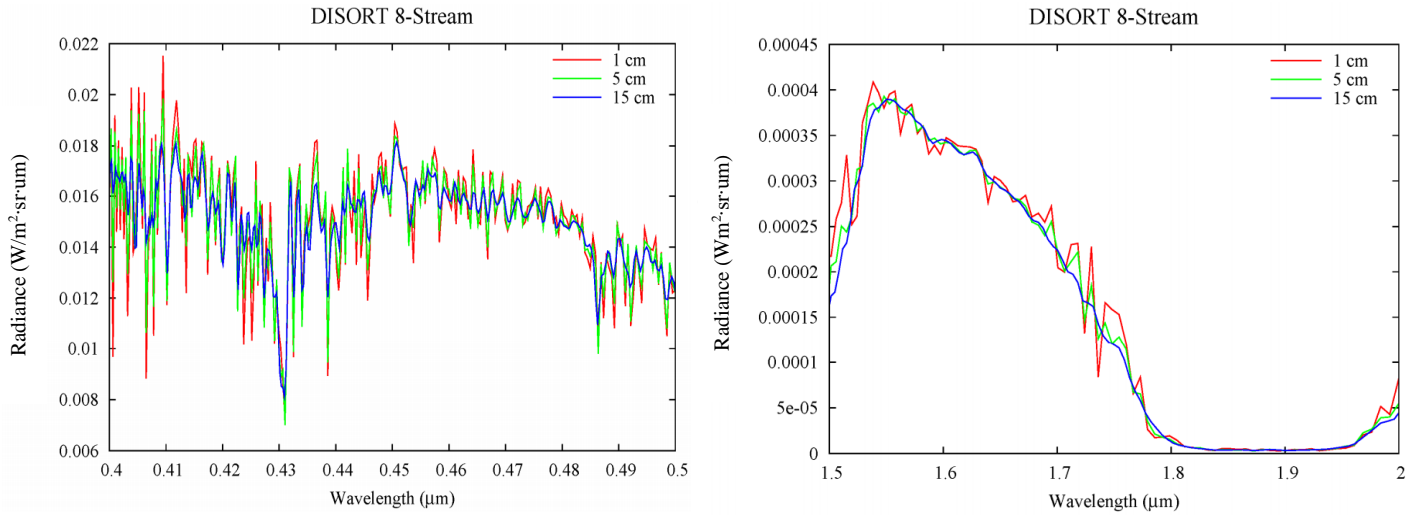and for the reduced sample used in this study. Error bar is 1 standard deviation.

697

698

699
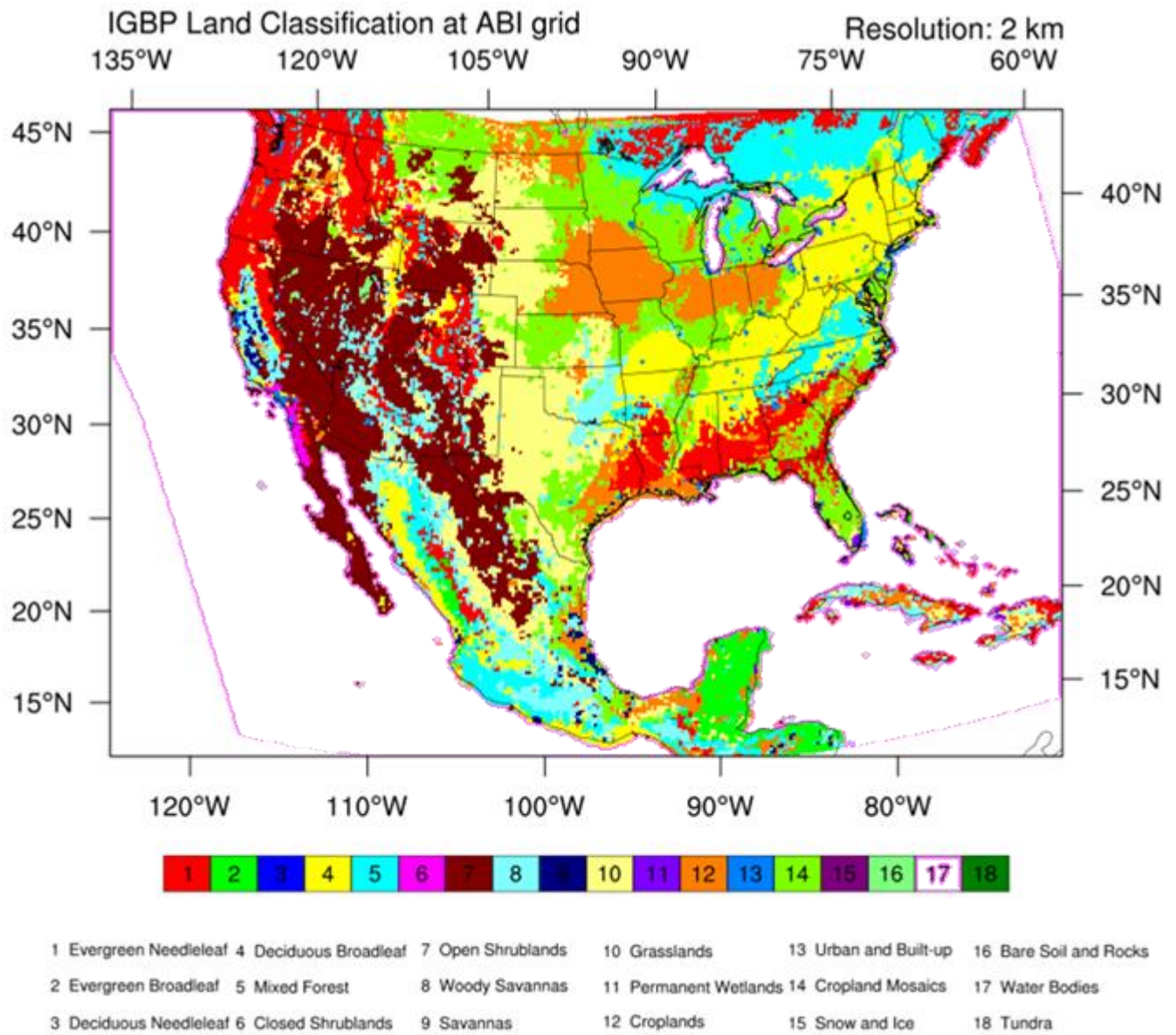
Figure 5. Re-mapped IGBP surface classifications over the CONUS at 2-km ABI grid.

701

702

703

704

705

Figure 6. Simulated Radiances from DISORT 8-stream (with 1, 5, and 15 cm^{-1} resolution band model for spectral range of 0.4 – 0.5 µm (left) and 1.5 – 2.0 µm (right).

706

707

708

709

710

711
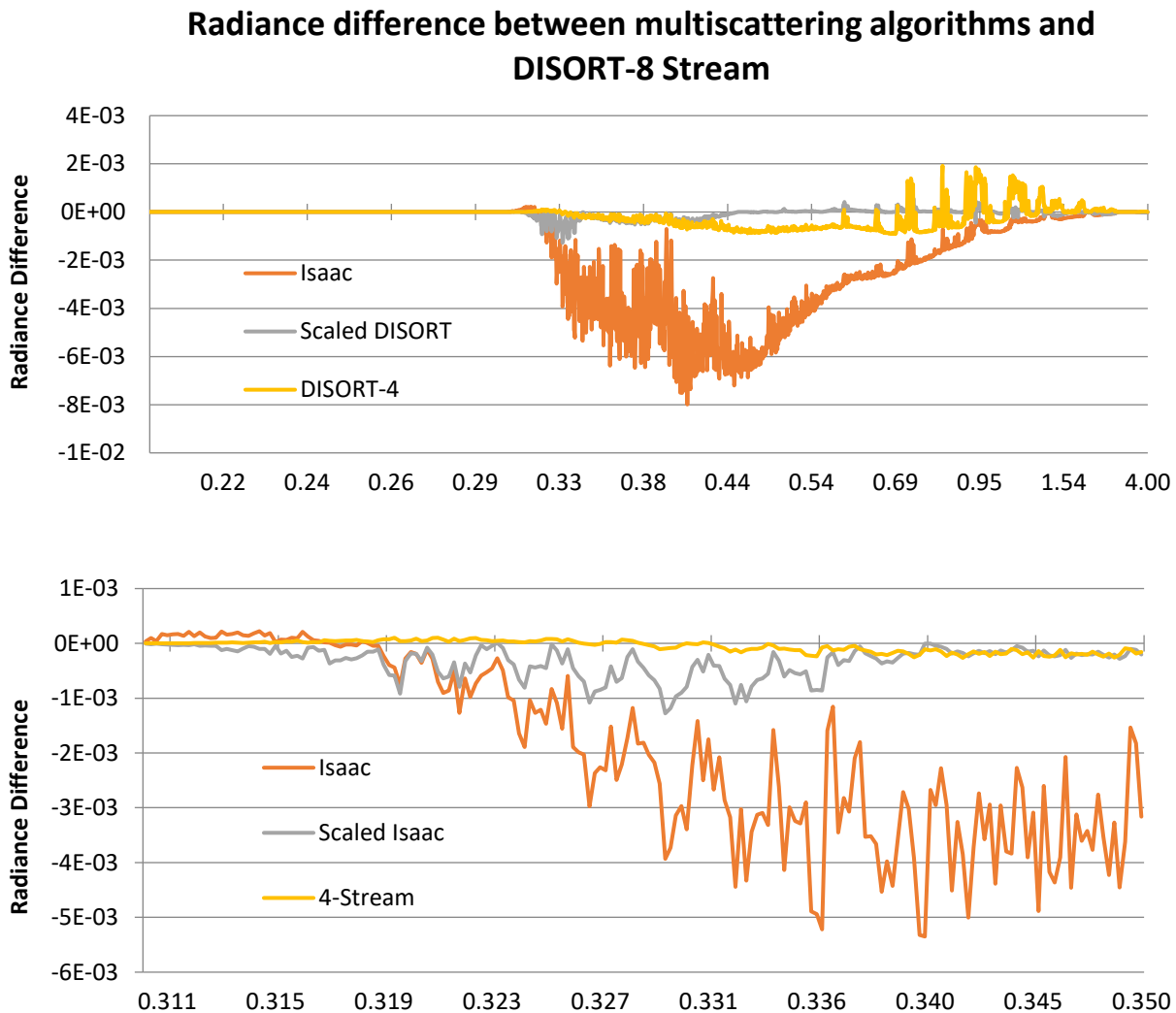
712

713

714 Figure 7. Radiance differences between various multi-scattering algorithms and DISORT-8 stream.

715 *Upper*: the whole simulated spectrum of 0.2-4 µm; *Lower:* zoom on 0.3-0.35 µm (Relative

716 Azimuthal Angle=1.9º, View Angle=76.3º, Solar Zenith Angle=87.2º).

717
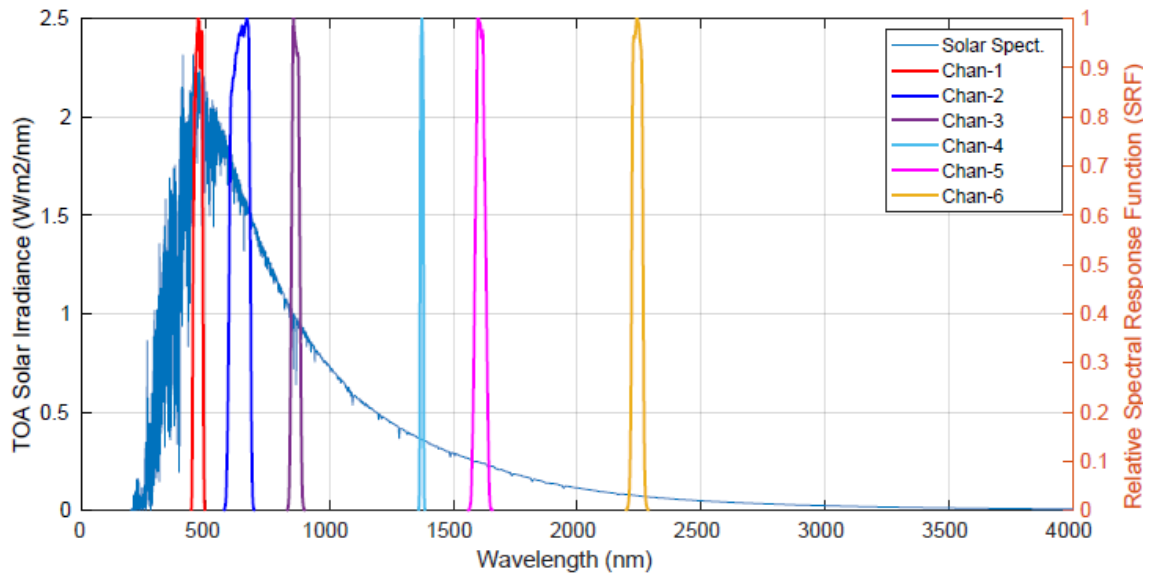
718

719

720   Figure 8. Locations of the six ABI channel SRFs. X-axis is wavenumber. Y-axis is solar irradiance.

721
722

723

724
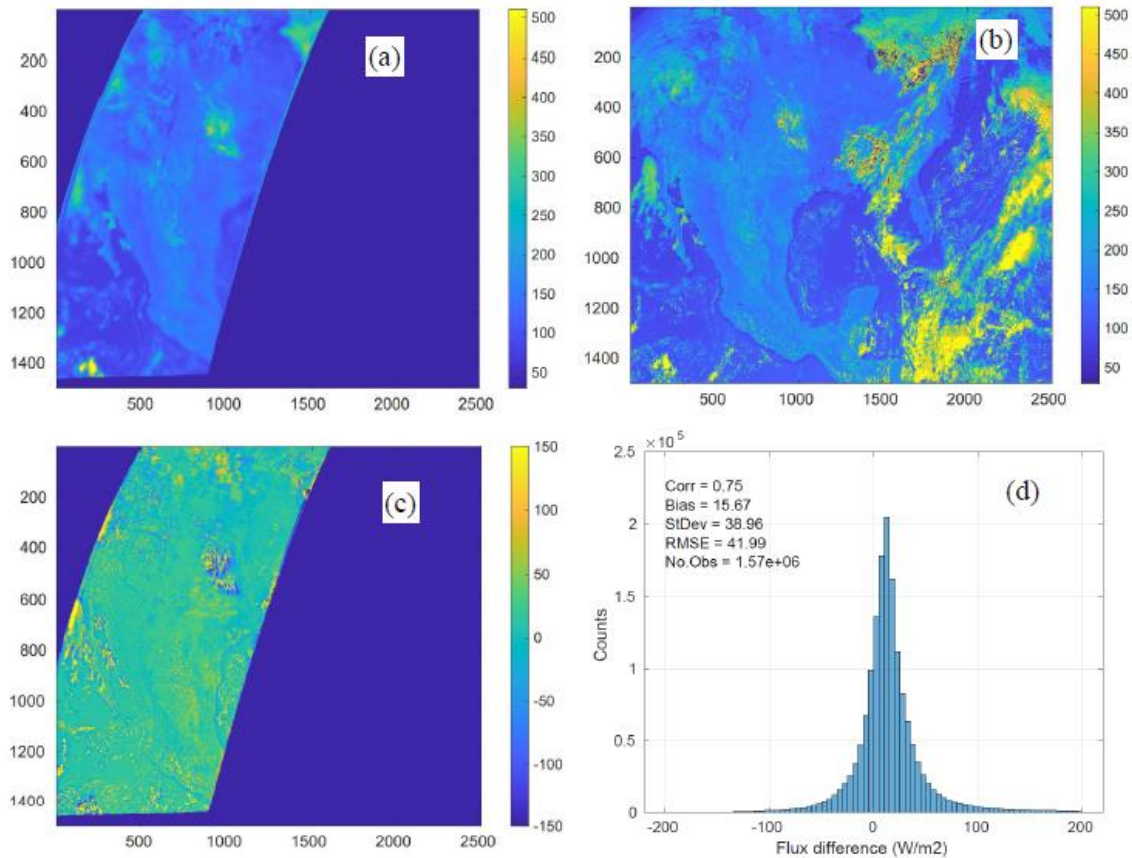
725

726   Figure 9. Comparison of TOA SW flux from ABI and CERES FLASHFlux for 2017/11/25, 17:57Z: (a)

727   CERES FLASHFlux Terra product (b) results from ABI with "separate channel" coefficients (c)

728   difference ABI-CERES FLASHFlux (d) histogram of ABI-CERES FLASHFlux differences

729   (this is the only case illustrated in this paper with data from FLASHFlux).

730

731

42

732
733
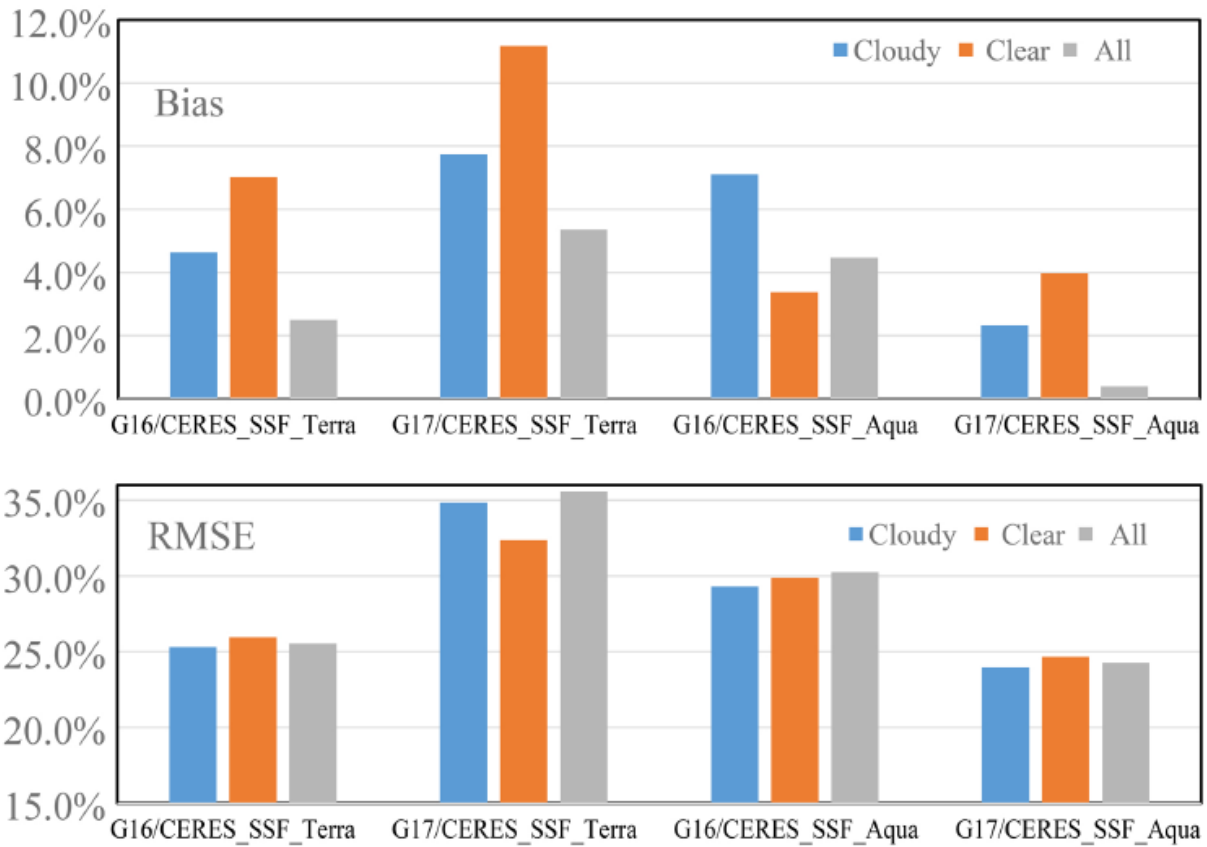
734
735   Figure 10. Statistics for relative Bias and RMSE. The y-axis is percentage. The x-axis is the case used in
736   the inter-comparison. Blue - cloudy orange - clear sky and t gray - all sky.
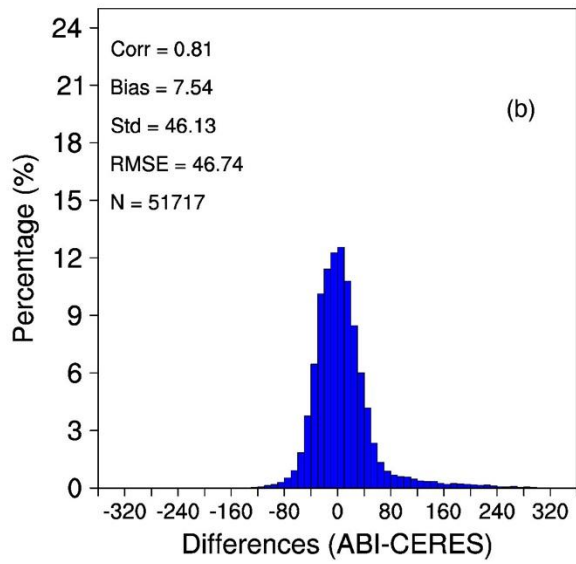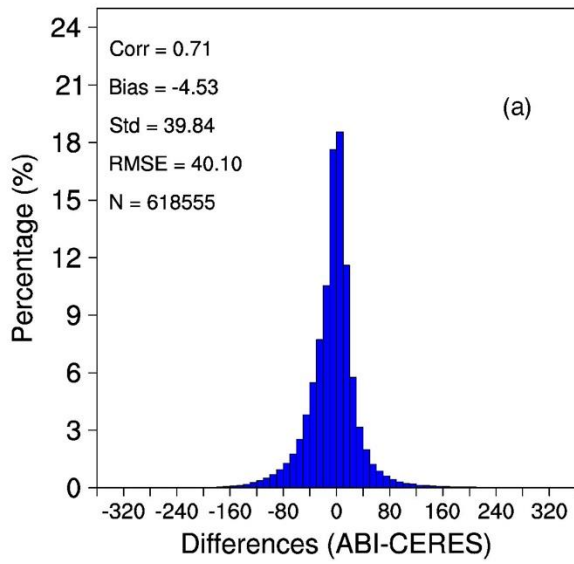
737
738
739
740
741
742
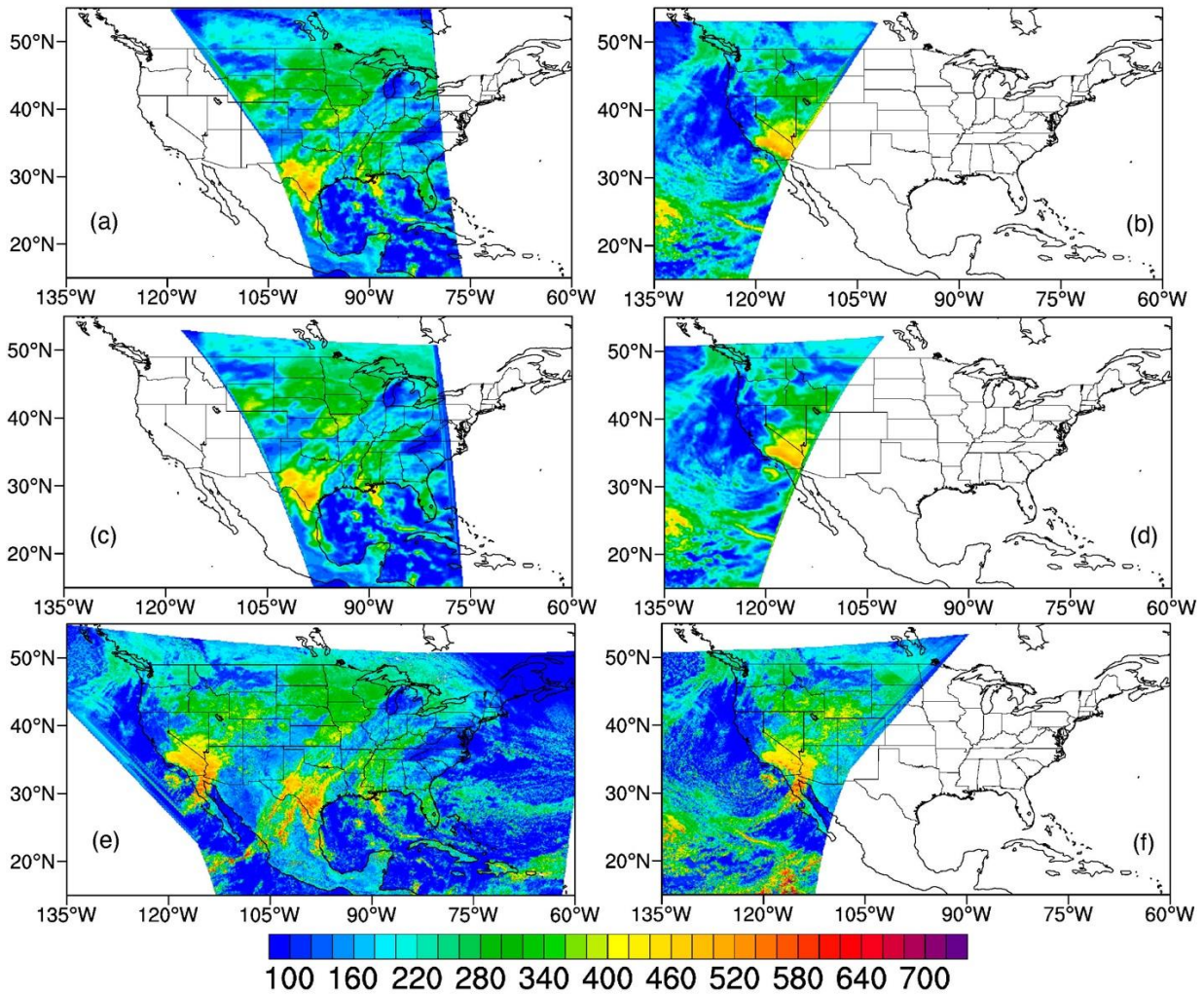
743
744
745   Figure 11. All sky TOA SW from: (a) CERES_SSF/Aqua (b) CERES_SSF/Terra (c) re-gridded

746   CERES_SSF/Aqua (d) re-gridded CERES_SSF/Terra (e) GOES-16 and (f) GOES-17, all on

747   12/26/2019 at UTC 19:36.

748
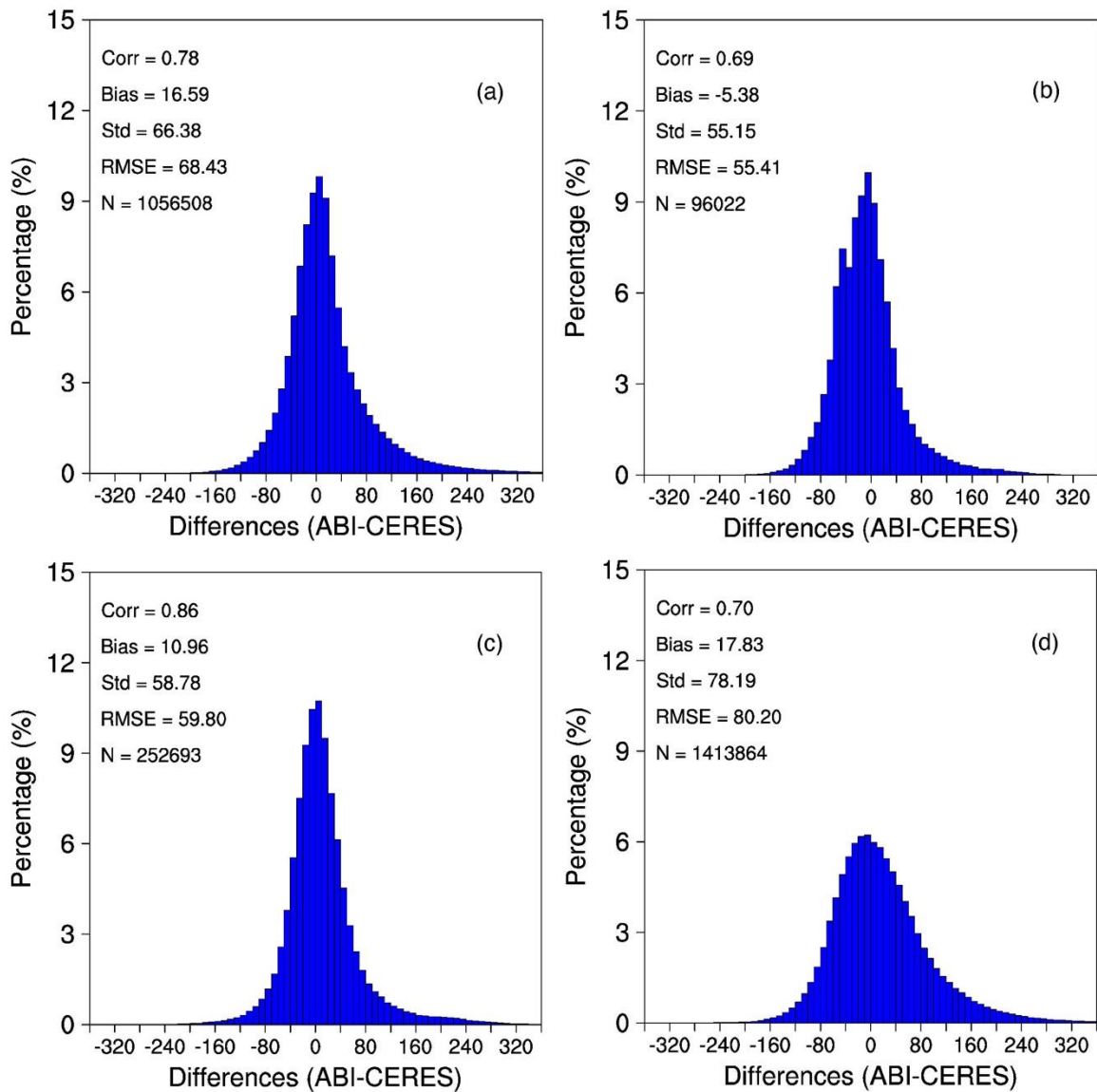
749

750
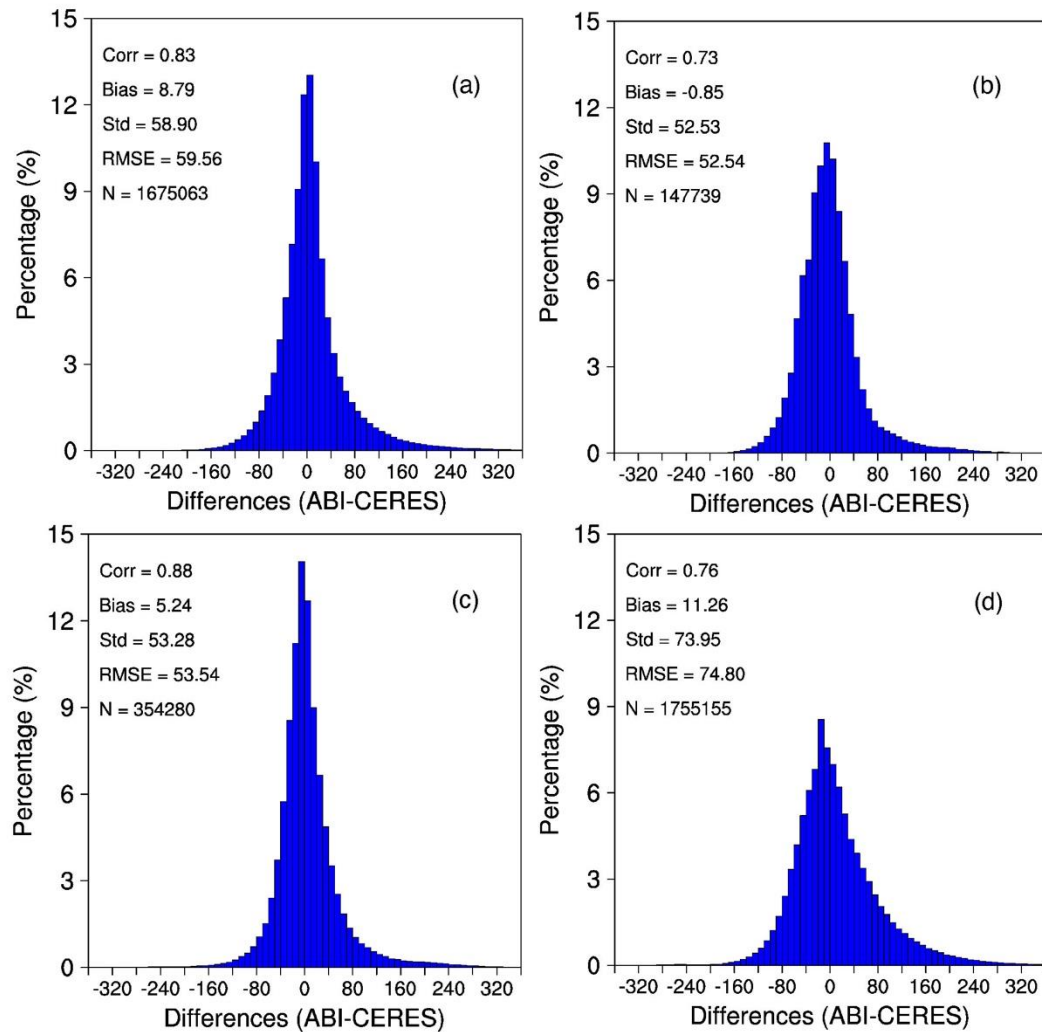
Figure 12. Frequency distribution of all-sky TOA SW differences between: (a) ABI on GOES-16 and CERES_SSF using Aqua (b) ABI on GOES-17 and CERES_SSF using Aqua (c) same as (a) using Terra (d) same as (b) using Terra. All observations were used (clear and cloudy) on 12/26/2019 at UTC 19:36.
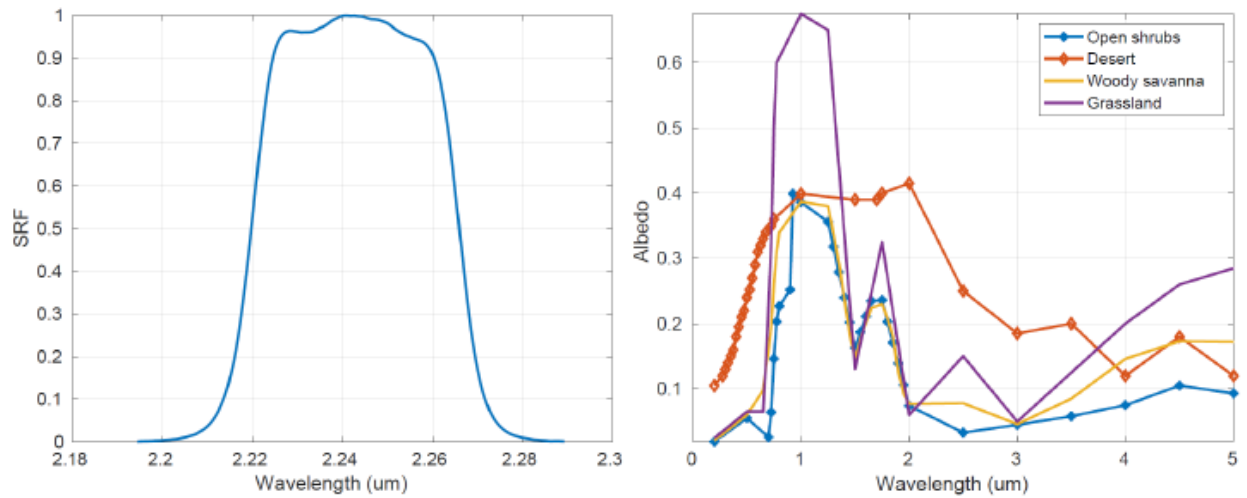
Figure 13. Same as Figure 11 but for clear TOA SW differences.

Figure 14. Same as Figure 11 but for cloudy TOA SW differences.

Figure 15. *Left:* Sensor response function for ABI channel 6; *Right:* Spectral albedo for desert and open shrubs. Desert albedo value is much higher than open shrubs at 2.2 µm.